A Measurement of the Extragalactic Background Light

Dennis Houlihan

(Dated: May 7, 2021)

The extragalactic background light (EBL) is the summed emission from all sources outside of the Milky Way Galaxy. An accurate measurement of the EBL can be used as a benchmark to test whether there are any components in excess of the integrated light from galaxies. Any discrepancies would imply the presence of sources of diffuse extragalactic emission that are currently unaccounted for, which is predicted to include light from the first galaxies in the universe. We have studied archival data from the Linear Etalon Imaging Spectral Array (LEISA) aboard the New Horizons spacecraft to determine whether it could be used to measure the EBL at wavelengths between 1.2 to 2.5 μm. We have empirically determined LEISA's sensitivity to diffuse brightness to be $\delta\lambda I_\lambda = 2 \times 10^6$ nW/m/sr in 1.5 second exposures, which essentially precludes the possibility of reaching EBL signals at the level of 10 nW/m/sr. These studies have allowed us to conclude that LEISA is not even capable of generating useful upper limits on the amplitude of the EBL at near-infrared wavelengths. We have also attempted to determine whether another New Horizons instrument, the Multi-Spectral Visible Imaging Camera (MVIC), could produce a good measurement of the EBL.

Introduction

The universe is home to a range of diffuse astrophysical backgrounds that, if measured accurately, can yield important insights into the process of cosmic structure formation. One such background is the extragalactic background light (EBL). The EBL is the total emission of all light outside of our Milky Way Galaxy at all wavelengths[1]. Specific wavelength ranges in the EBL are remnants of specific emission sources. One component of this background is the Cosmic Microwave Background (CMB), which was emitted shortly after the Big Bang. It is a prime example of how fruitful diffuse background studies can be as it is a major source of information about the early universe[2].

The infrared component of the EBL is referred to as the Cosmic Infrared Background (CIB). It is believed that the CIB is dominated by redshifted starlight[3]. Just as the CMB provides information on the early universe, measuring the CIB could potentially provide new information on stellar and galactic processes as well as reveal other sources of emission[4]. More specifically, a precise measurement of the EBL can be used as a valuable test where integrated light from discrete sources such as galaxies can be compared[2]. From this, constraints on models of galaxy formation and evolution[1], star formation, and metal and dust production[5] can be determined. Other potential results include discoveries such as the signature of recombination from the epoch of reionization and the presence of intra-halo light in the intragalactic medium[4].

Prior ground-based measurement of the CIB has proven to be extremely difficult as there are a number of diffuse foregrounds that must be taken into account, as well as atmospheric extinction (absorption), scattering, and airglow emission[6]. The three most prominent foregrounds are the integrated star light (ISL), zodiacal light (ZL), and the diffuse galactic light (DGL)[4]. Foreground contribution is illustrated in Equation 1[2], which governs the brightness in an arbitrary image of the astronomical sky outside of Earth's atmosphere.

$$\lambda I_\lambda^{\mathrm{meas}} = \lambda I_\lambda^{\mathrm{IPD}} + \lambda I_\lambda^* + \lambda I_\lambda^{\mathrm{RS}} + \lambda I_\lambda^{\mathrm{DGL}} + \epsilon I_\lambda^{\mathrm{EBL}} + \lambda I_\lambda^{\mathrm{inst}} \quad (1)$$

$\lambda I_\lambda^{\mathrm{IPD}}$ is the brightness associated with interplanetary dust (IPD), λI_λ^* is the brightness from resolved stars, $\lambda I_\lambda^{\mathrm{RS}}$ is the brightness from residual starlight of stars too faint to detect individually, $\lambda I_\lambda^{\mathrm{DGL}}$ is the brightness from the DGL, ϵ is a factor that accounts for absorption in galactic dust, and $\lambda I_\lambda^{\mathrm{inst}}$ is the instrument contribution. We can isolate $\lambda I_\lambda^{\mathrm{EBL}}$ in three steps[7]: remove the effect of λI_λ^* by masking bright stars; subtract the diffuse components to isolate the diffuse residual component $\lambda I_\lambda^{\mathrm{resid}} = \epsilon I_\lambda^{\mathrm{EBL}}$; and correct the mean residual intensity for the effects of galactic extinction (determine value of ϵ) to yield $\lambda I_\lambda^{\mathrm{EBL}}$.

One way around the brightest of these foregrounds is the use of instruments aboard New Horizons[9], a NASA spacecraft sent to survey Pluto, its moons, and other objects in the outer solar system. In addition to their original purpose, New Horizons instruments can be used for astronomical measurements. This provides a rare and exciting opportunity to measure the EBL from an outer solar system vantage point that is free from the Earth's atmosphere and substantially decreases the effect of the ZL. The goal of this capstone project was to make a good measurement of the CIB in the near infrared spectral range with archival data from the New Horizons instrument known as the Linear Etalon Imaging Spectral Array (LEISA)[9].

The first phase of this project focused mainly on learning about LEISA's instrumentation and data pipeline, performing preliminary data assessment and cuts, as well as finding where the image is pointing in order to find stars. These were important preparatory steps because in order to make accurate measurements of

the CIB, one needs to understand how LEISA's parameters affect the data and if the data we use is adequate for our purposes. Knowing where the images are pointed is also extremely important because the light contribution of stars is needed to be taken into account.

The second phase of this project focused on measuring the sensitivity of LEISA in order to conclusively determine whether a measurement of the EBL is feasible. By performing point-spread function fitting photometry and calibrating the spectrum data, we were able to determine that LEISA was not capable of yielding accurate measurements of the EBL. After LEISA, we tried moving onto another New Horizons instrument called the Multi-Spectral Visible Imaging Camera (MVIC). As with LEISA, we focused on learning about MVIC's instrumentation, performed cuts to the data sets, and attempted to determine where the instrument was pointing so we could locate stars and mask them.

Foregrounds to the EBL

The ISL is the total sum of light emitted from stars within the Milky Way Galaxy[8] and corresponds to both λI_λ^* and λI_λ^{RS} from Equation 1. It is easy to account for brighter stars, however, there are faint stars that are below the detection threshold of a given image that still contribute to this foreground. Taking advantage of real observations and star population models such as the TRILEGAL model[2] will be needed to estimate the faint stars contribution.

The ZL is caused by solar light scattered by interplanetary dust particles within the plane of the ecliptic[2]. This dust disperses after being ejected from their parent bodies[2] such as comets, asteroids, and Edgeworth-Kuiper Belt objects. The ZL is concentrated within the plane of the ecliptic and is fainter outside of it[8]. Furthermore, IPD in general is more prominent within the inner solar system, as measurements from Helios, Galileo, and Pioneers 8/9 show a steep decline in IPD density outside of 1AU[4] and confinement to within $30°$ of the ecliptic plane.

In a similar way to the IPD, dust along the plane of the Milky Way scatters light from stars within the galaxy. The resulting foreground is known as the DGL (λI_λ^{DGL}). As the ZL is brightest along the ecliptic, the DGL is brightest in the galactic plane and fainter at higher galactic latitudes[7]. It is important to note that the DGL is due to dust in interstellar space, not interplanetary space. Therefore, outer-solar system location does not mitigate this light contribution and no where in the sky can we ignore this foreground.

The LEISA Instrument

Launched on January 19, 2006, the New Horizons spacecraft was NASA's first mission to explore Pluto and its moons Charon, Nix, and Hydra[9]. It is currently in an extended mission focused on Kuiper Belt science at heliocentric distances of beyond 50AU[4] and will continue on this mission until at least 2021.

One of the core instruments aboard the New Horizons spacecraft is *Ralph*[9], a visible/near-IR multispectral imager. It consists of a telescope that feeds two sets of focal planes that are intended to provide color, composition, and thermal maps for the surfaces of Pluto and its moons[9]. At one of these focal planes is MVIC and LEISA[10].
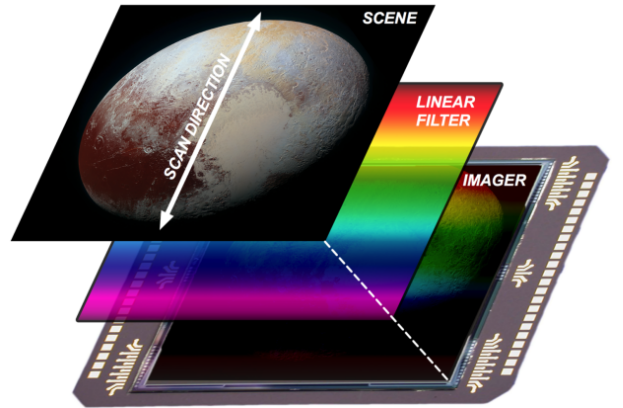

Figure 1: A schematic of the how the LEISA instrument works[11]. As the scene (in this case, Pluto) moves along the scan direction, the imager records many frames of video in sequence, imaging each part of Pluto though each segment of the linear filter and building up a spectral map of the entire object.

LEISA is a wedged filter infra-red spectral imager with a $256{\times}256$ pixel array whose filter is separated into two pieces: a high and low spectral resolution segment bonded together. The wavelength range of the sensor is 1.225-2.5μm for the low resolution segment and 2.1-2.25μm for the high resolution segment[12]. The wavelength of the filter varies along each row, meaning each row measures a specific wavelength. Scanning along the array allows for the imager to produce a spectral map of the target. Figure 1[11] shows a general schematic of how LEISA works.

LEISA's wavelength range can be used to detect near-IR sources such as redshifted starlight in galaxies. This is especially valuable because measurements from 1-3μm have been very challenging on Earth[5] due to the bright foregrounds mentioned. LEISA also has a large field of view ($0.9° \times 0.9°$)[10] so it can probe a larger area of the sky and provide a better sense of the EBL's nature.

Although its vantage point avoids the bright ZL, LEISA's parameters are not optimal for measuring the EBL. In Table I, LEISA's parameters are listed. For example, LEISA's spectral resolution (R = 240) means that it has a poor per-pixel sensitivity[4]. This in turn requires a significantly longer integration time ($\sim$1 day as compared to $\sim$1 hour for MVIC)[4] to make a constraining measurement of the CIB. This coupled with the short

LEISA Instrument Parameters	
FOV:	$0.9° \times 0.9°$
Single Pixel FOV:	12.38 arcsec $\times$ 12.38 arcsec
Pixel Size:	$40\mu m \times 40\mu m$ Pixels
Ralph Telescope Aperture:	75mm
Ralph Telescope Focal Length:	657.5mm
Spectral Resolution:	$\lambda/\Delta\lambda = 240$
Dark Current:	40 counts/second
Per-pixel Sensitivity:	$6 \times 10^4 nWm^{-2}sr^{-1}$
Expected CIB Signal:	$10\ nWm^{-2}sr^{-1}$
In Track FWHM:	1.40 ± 0.13 Pixels

Table I: Tabulated parameters for LEISA and Ralph. All values were found in the Ralph instrument paper[10].

integration times of the images from the publicly available data-sets[13,14] made it almost impossible to detect stars with magnitudes ranging from 6-10. This issue is outlined in more detail in the later sections.

Preliminary Data Cuts

Before I could start the analysis, data assessment and cuts were performed to ensure the images used are adequate for our purposes. Factors such as exposure time, type of image, and the presence of bright objects were all considered when determining whether to validate an image. The first thing I did was write a Python code that looped through the LEISA data sets and printed the values for exposure time as well as other header keywords that provide descriptions of the image.

Once I had a list of these keywords, I immediately cut images with exposure times less than four seconds from consideration. Images with longer exposure times are desirable because LEISA's sensitivity is very poor, the EBL is very faint, and four seconds is the maximum exposure time in any LEISA image. I then checked each image for any defects or bright objects that may hinder our ability to measure the faint EBL signal. Fortunately, each image with exposure time of four seconds did not have such defects. After completing the preliminary cuts, I was left with eight images deemed acceptable: two images from the Pluto Encounter Phase and six images from the Pluto Cruise Phase of the New Horizons Mission[13].

Post-Reduction Analysis

One step in this project was to exclude the brightness from the resolved starlight, or λI_λ^* from Equation 1. To do this, I needed to implement image masks to remove signals from unwanted sources. Masking is the process of identifying and ignoring stars or other sources of light that are near or brighter than the detection threshold from an image[7]. One can identify stars using various

catalogues that are publicly available, such as the Gaia DR2 catalog[18]. Successfully implementing masks in our images ensures that I can effectively ignore bright contributions to the sky brightness from stars, hot pixels, and other defects in our images.

Before masking the stars, we first needed to compute the celestial coordinates for each pixel in the images. Then, I can compare the stars found in the image with the objects in the Gaia DR2 catalog. From there, I can mask the appropriate pixels in the image. This procedure was not completed due to complications arising from the instrument's quaternion data and LEISA's poor sensitivity that prevented us from both locating and detecting the stars in the images.

Instrument Pointing

Calculating the instrument pointing is crucial for our goal of measuring the EBL. As stated before, accurate astrometric data allows us to locate and mask bright stars in the images. LEISA utilizes rotation quaternions to allow the user to calculate the J2000 cartesian pointing vectors of each pixel[12]. In extension 3 of each FITS file, the cartesian pointing vectors of each pixel in the instrument reference frame is stored as a $256 \times 256 \times 3$ array. In extension 7 of each FITS file, the ephemeris time and quaternion for the center of each frame is stored as a $5 \times N$ array, where N is the number of frames in the image. By rotating the pointing vectors by the given quaternions, the cartesian J2000 vectors can be derived. From there, the Right Ascension and Declination coordinates of each pixel can be calculated by converting these vectors into polar coordinates.

Right Ascension and Declination are celestial coordinates that describe an object's position on the sky[19]. Just as cities need longitude and latitude coordinates, each object in the sky needs Right Ascension and Declination coordinates to fix its location. Because Right Ascension and Declination are constantly changing due to Earth's precession, these coordinates are referenced to a specific epoch. J2000 is presently the standard Julian epoch that is based on Julian years of exactly 365.25 days. J2000 refers to January 1, 2000, noon TT (Terrestrial Time)[19].

Quaternion Rotations

To understand how to rotate a vector with a quaternion, one must first understand what a quaternion is. A quaternion is a 4-element vector composing of one real and three complex elements. Unlike Euler angles that rotate vectors by a series of rotations around the X, Y, and Z axes, a quaternion rotates a vector about a rotational axis, that is not necessarily the X, Y, or Z axis[20]. First, let the standard cartesian basis **i**, **j**, **k** satisfy the

following condition:

$$\mathbf{i}^2 = \mathbf{j}^2 = \mathbf{k}^2 = \mathbf{ijk} = -1 \tag{2}$$

We can then define a quaternion as the sum of a scalar and a vector:

$$\bar{q} = q_0 + \mathbf{i}q_1 + \mathbf{j}q_2 + \mathbf{k}q_3 = q_0 + q \tag{3}$$

where

$$q = \mathbf{i}q_1 + \mathbf{j}q_2 + \mathbf{k}q_3 \tag{4}$$

For LEISA, and for aerospace engineering in general[20], a special normalized quaternion $q_0 = \cos\frac{\alpha}{2}$ and $q = \hat{e}\sin\frac{\alpha}{2}$ is used, where α is the rotational angle and $\hat{e}$ is the rotation axis. Say we have a vector that we want to rotate $\bar{v}$:

$$\bar{v} = a\mathbf{i} + b\mathbf{j} + c\mathbf{k} \tag{5}$$

To perform this rotation, we have to take the tensor product between the vector, the quaternion, and the complex conjugate of the quaternion. It is important to note that quaternions are non-commutative[20], which means that the product of two quaternions depends one what quaternion is on the left and what is on the right. In other words, order matters. So if we define $\bar{w}$ as the resulting vector of $\bar{v}$ being rotated by the quaternion $\bar{q}$, then it should look like:

$$\bar{w} = \bar{q} \otimes \bar{v} \otimes \bar{q}^* \tag{6}$$

Where $\otimes$ denotes a tensor product. For LEISA, $\bar{q}$ would be the quaternion stored in extension 7 of the FITS file, $\bar{v}$ would be the cartesian pointing vector in the instrument fixed body frame, and $\bar{w}$ would correspond to the resulting cartesian J2000 pointing vector. The next step is to use the J2000 pointing vectors to calculate the Right Ascension (α or RA) and Declination (δ or Dec) coordinates of each pixel. As a note, I will be using RA and Dec in text but α and δ in equations for Right Ascension and Declination, respectfully. To calculate RA and Dec, we must convert our J2000 pointing vectors from cartesian to polar coordinates. If we think of the unit circle, RA would be the azimuthal angle while Dec would be the polar angle. Therefore, we can relate the J2000 cartesian coordinates (X,Y,Z) to the polar coordinates (α,δ):

$$X = \cos\alpha\cos\delta \tag{7}$$

$$Y = \sin\alpha\cos\delta \tag{8}$$

$$Z = \sin\delta \tag{9}$$

Solving for δ in Equation 9, we see that Dec can be expressed as:

$$\delta = \arcsin Z \tag{10}$$

By dividing Equation 8 by Equation 7, we can find an expression for RA:

$$\alpha = \arctan\frac{Y}{X} \tag{11}$$

I attempted to perform this procedure for each pixel in each frame of the LEISA images, but found the third imaginary, or z-component, of each quaternion was zero. Without a full quaternion, we were not able to calculate pointing data for every frame in the images.

Missing Quaternion Data

At first glance, having a zero z-component was nonsensical when comparing it to the quaternion given in the header, which corresponds to the middle frame of the image. The quaternions in the headers all had non-zero z-components. To make sure that this was a case of missing data, I performed several tests.
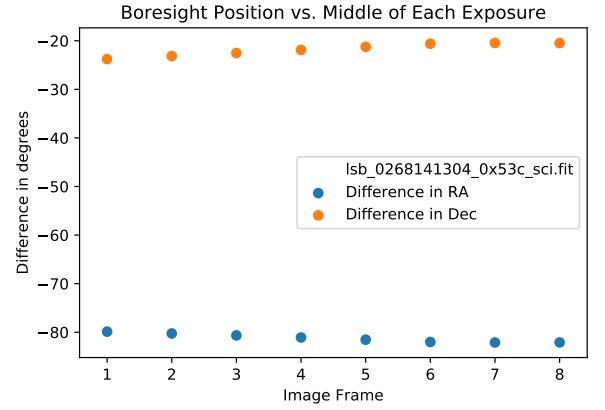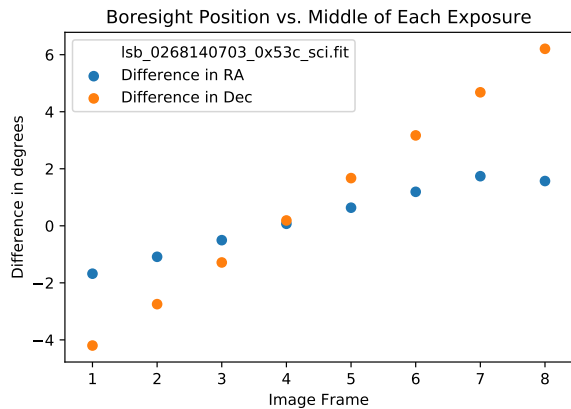

Figure 2: Comparison of the boresight Right Ascension and Declination coordinates given in the header of the FITS files with calculated coordinates of the middle of each exposure using approach (1). The differences are substantial, implying the zero component of the extension quaternion is incorrect.

My tests were to rotate the vectors two different ways: (1) using the quaternions from the extension for each frame; (2) using the scalar and first two imaginary components of each quaternion from the extension with the z-component of the image header's quaternion. I then calculated the J2000 RA and Dec coordinates. Each header has a set of boresight RA and Dec coordinates that refer to the center of the middle frame. In each scenario, I compared the boresight coordinates that were given in the header with my computed J2000 RA and Dec coordinates of the middle of each exposure. Figure 2 shows the results of the approach (1). Considering the field of view of LEISA is $0.9° \times 0.9°$, these differences are considerable and prevent me from calculating accurate astrometric data with the given quaternions.

Figure 3: Comparison of the boresight Right Ascension and Declination coordinates given in the header of the FITS files with calculated coordinates of the middle of each exposure using approach (2). One can see the differences are minimized in the middle exposure.

Figure 4: Comparisons of Vega's position with the calculated position using approach (2). The differences in the accepted and calculated values are smallest in the middle frames and increase the farther away from the middle frames they are. This is expected as the quaternion from the header corresponds to the middle exposure of the image.

Figure 3 shows the results of using approach (2). This is a "band-aid" approach, which yields results that agree near the center frame, but get worse the further from the center exposure you go. I would expect this behavior if the third component of the quaternion information should be updated in each exposure; since the quaternion reported in the header is referenced to the middle integration, assuming that value should minimize the discrepancy. This clearly shows that information is missing, and the header value is not a complete description.

Another test I conducted was to track the star Vega in the image labeled lsb_0397097519_0x53c_sci.fit from the "Cruise to First KBO Encounter" data set[14]. This image was not validated for our purposes, we used this solely for this test. In this image, the star Vega is being scanned in a window as a slow scan test. For every ten frames, starting at frame 40, I recorded Vega's position on the image, and recorded my calculated RA and Dec coordinates for each using approach (2). Figure 4 above shows the difference between the calculated position of Vega for each frame (the missing data points are due to Vega passing through a very noisy section of the image, making it difficult to see where it was). Again, the differences are smaller towards the middle frames and get larger the farther from the middle frames you go. This is the same trend seen with the image boresight test.

A report about the missing quaternion data was made and sent to the manager of the Small Bodies Node of NASA's Planetary Data System, Dr. Ludmilla Kolokolova. We were told that the issue would be studied further and they will inform us as well as other LEISA users of the updates in the data set done to resolve the problem. However, no new information has been shared as of yet and no timetable was given for how long fixing the quaternion data would take.
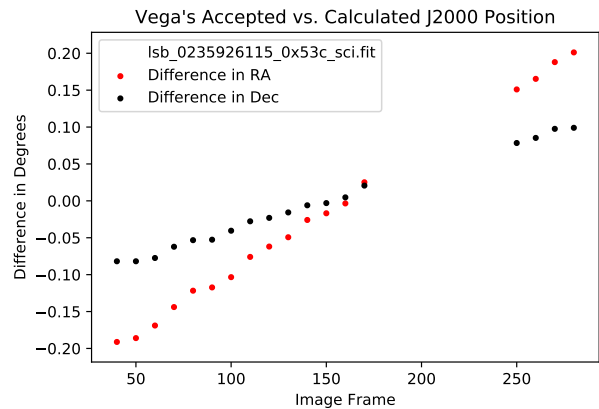
Searching for Stars in LEISA Images

While the missing quaternion data has significantly limited our ability to calculate accurate J2000 coordinates, there was still some work we were able to do. One thing was to find and mask any stars found in the middle frame. As shown before with image boresight and Vega test, the difference between the calculated and accepted values were minimized in the middle frames of the images. So ideally, we would be able to find stars in the middle frame at least.

Figure 5 shows an image from the Pluto Cruise data set. Simply looking at the image, no stars are apparent, which is true for our entire validated image set. The bright spots are due to instrument noise that is seen in each LEISA frame. However, I was able to see Vega in the prior test because Vega is a very bright star with an apparent V magnitude of about 0.026[21]. Fainter stars of magnitudes ranging from 6-10 are much harder to view due to LEISA's poor per pixel sensitivity. Because of this, programs such as Source-Extractor could not detect objects within the image. Source-Extractor simply searches an image for especially bright spots to identify objects and outputs various parameters such as flux, position, etc. for the identified objects[22]. With the stars very faint, and some noise very bright, we would run the risk of the program identifying noise as objects and ignoring the actual stars completely. Ultimately, we had to search for stars ourselves.

Instead of trying to find stars in the image and compare their coordinates to stars in a catalog, I decided to compare the positions of objects in the Gaia DR2 catalog[18] with each pixel in the middle frame of our images. I first created a query for objects within a box with length 0.9° (field of view of LEISA) centered
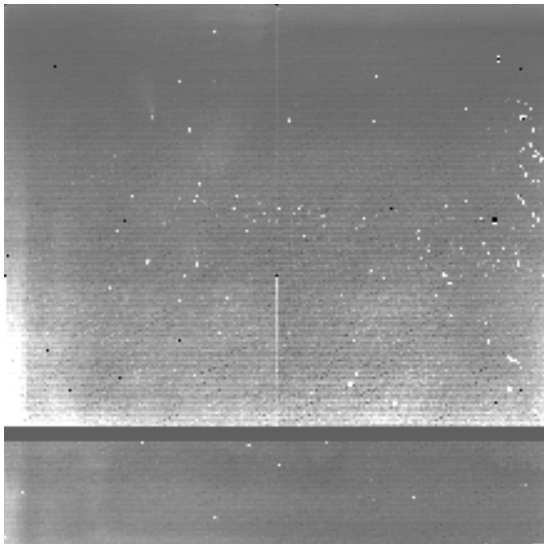
Figure 5: The image lsb_0235926115_0x53c_sci.fit. The bright spots are instrument noise exhibited in every LEISA frame. There is also a considerable gradient exhibited in the low spectral resolution segment of the image.
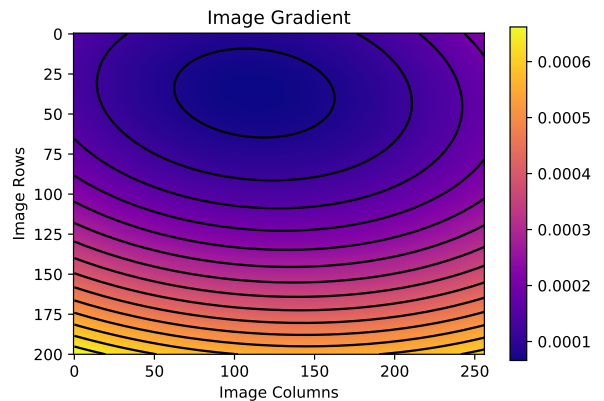

Figure 6: Data fitted to a two dimensional parabola for the image lsb_0235926115_0x53c_sci.fit's low spectral resolution segment in the Pluto Cruise data set. The gradient is predominantly exhibited in the image's y-direction.

at the boresight position listed in the header. I then ran a Python code that calculated the distance between the Gaia objects and each pixel in the image frame. It then paired each Gaia object with the closest pixel in the frame. Searching these pixels, I could not find any significant bright pixels that would usually indicate a star.

To help us see the stars, we attempted a few different techniques. One technique was to subtract the first frame of the data cube from the middle exposure in the hope that it would subtract the common noise/defects, and hence make the stars more apparent. This did not make the stars any more noticeable, even after adjusting the scaling of the image frame. Next, we tried to sum all the frames in the data cube in the hopes that the stars would create a bright trail as the instrument moved across the field. Checks were made to make sure no especially bright or defective frames were included in the sum. Despite this, there were no trails exhibited in the image.

Finally, I attempted to correct the gradient that was exhibited in the low resolution segment of the images. To do this, I fit a two dimensional parabola to the image data. I then subtracted the fitted data from the original image. Figure 6 shows the fitted data for the image lsb_0235926115_0x53c_sci.fit from the Pluto Cruise data set. Unfortunately, correcting the gradient also failed to yield any change in the stars' appearance.

LEISA Sensitivity Measurement

In order to conclusively determine the feasibility of a measurement of the EBL with LEISA, I performed Point-spread function (PSF) fitting photometry to measure the instrument's sensitivity. We know that the expected brightness of the EBL[2] is about $10\,\mathrm{nW/m^2/sr}$, so if we find that LEISA is not sensitivity to signals that faint, then we can conclude that LEISA is not fit to make a measurement of the EBL.

PSF Photometry is the process of measuring the apparent brightness of objects in specified ranges of wavelength in and near the optical band[23]. This is done by calculating the PSF weighted average of the flux of an object. A PSF describes an instrument's response to a point source or point object. It often shows as an extended blob representing a point source and the degree of such blurring reflects upon the quality of the imaging system (less blurring is good).

The LEISA image chosen to perform the photometry on is the same image used in the Vega test: lsb_0397097519_0x53c_sci. This image was chosen because it features several frames that track the star Vega, which is the only star able to be detected in our data set. Not only can we measure its brightness, but Vega also serves as an excellent point source, which helps in constructing an accurate PSF.

Constructing a PSF

To construct a PSF, I followed the procedure outlined in an astropy tutorial[24]. Astropy is collection of software packages written in the Python programming language and designed for use in astronomy. First, I created a summed image comprised of several frames. Since this image is in scanning mode, Vega "moves up" the image in each successive frame. So instead of only using one frame of Vega to construct my PSF, I summed frames #40, 56, 71, 88, and 103 so that Vega would be spaced out in the same image. This allowed me to include
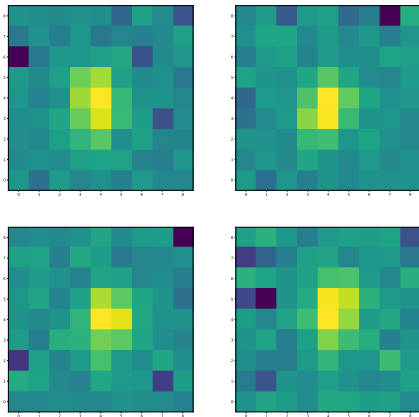
Figure 7: Four of the star cutouts from the summed image.

multiple frames of Vega to construct a PSF. I then made a table of these stars using the function "find_peaks"[24] which records the positions of peaks that lie outside of a set threshold from the background.

The data with which I build the PSF must have the background subtracted. Here I used the function "sigmaclipped_stats"[24] to retrieve the median value and used that as the background level. I then used the function "extract_stars"[24] to extract cutout images centered on stars defined in the input table. From there, I used the function "epsf_builder"[24] to create a PSF to use for our photometry. Figure 7 shows four star cutouts and Figure 8 shows the constructed PSF.
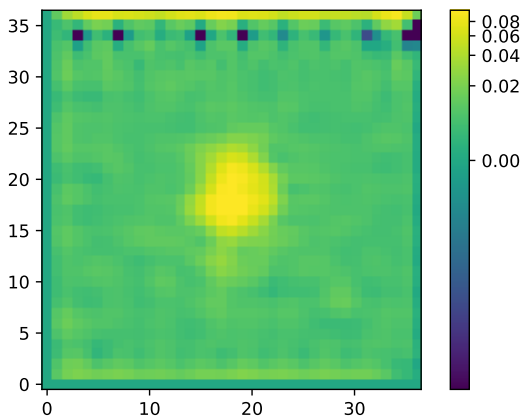

Figure 8: The constructed PSF using the star cutouts from the summed image.

Performing PSF Photometry

There are a few steps that needed to be taken to perform PSF photometry. First, I needed to isolate Vega in each frame so to measure the flux of the star. One way to do this is to use an astropy function called

"DAOStarFinder"[24]. This function detects stars and retrieves the centroid positions in an image by searching for local density maxima that have a size and shape similar to a 2D Gaussian function. Once the centroids of Vega are retrieved, I can make a small box around each and take the PSF weighted average of the flux and wavelength of each box by using Equations 12 and 13.

$$\langle F \rangle = \frac{\int F(x,y)P(x,y)dxdy}{\int P(x,y)dxdy} \quad (12)$$

$$\langle \lambda \rangle = \frac{\int \lambda(x,y)P(x,y)dxdy}{\int P(x,y)dxdy} \quad (13)$$

With $F(x,y)$ being the flux in the box, $P(x,y)$ being the PSF I created, and $\lambda(x,y)$ being the wavelength data from the wavelength extension of the FITS file. From this, a spectrum can be found by plotting the weighted flux vs. the weighted wavelength. The next step would be to calibrate this data with an accepted spectrum of Vega. This is an important step because it serves as a reference that tells whether the calculated data is correct and can show mistakes that would have otherwise been undetected.

In order to use the astropy star tracking function, I created stamps around Vega in each frame. This decreased the chance of the function identifying objects and noise other than Vega. Vega oscillates along the y-axis and travels up the x-axis of the image. So I made the y length fixed by subtracting 20 pixels from its minimum y value and adding 20 pixels to its max y value. For the x-direction, I made the length 30 pixels centered around the first x value recorded. Then for each frame, I added 1 pixel to the max and min x value of the stamp so it would follow the star as it moves up the x-axis. This procedure was repeated with the wavelength data extension.

For each stamp, I used the "DAOStarFinder" as outlined before to detect Vega and find its centroid. Unfortunately, there were some misidentifications that I had to manually go through and delete. After that, I created boxes of length 3 pixels around the x and y coordinates of the centroids. I repeated the procedure for the wavelength extension. Within those boxes I performed the PSF weighted average using Equations 12 and 13. I also calculated the weighted average of flux error. The error of the flux is given in Extension 5 of the FITS file.

$$1\,\mathrm{ergs/cm^2/s/sr/\text{Å}} = 10^{-3}\,\mathrm{W/m^2/sr/\text{Å}} \quad (14)$$

$$1\,\mathrm{W/m^2/sr/\text{Å}} = 10^9\,\mathrm{nW/m^2/sr/\text{Å}} \quad (15)$$

$$\lambda I_{final} = I_{initial} \times \lambda[\text{Å}] \times 10^6\,\mathrm{nW/m^2/sr/\text{Å}} \quad (16)$$

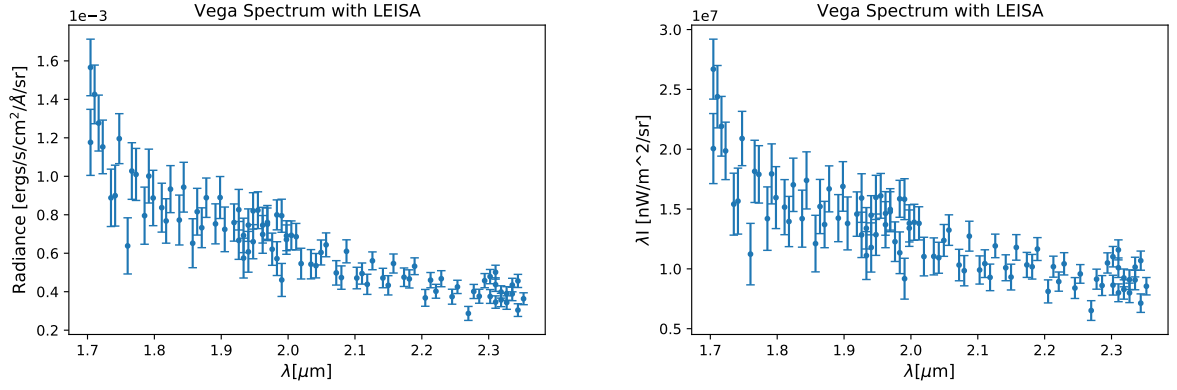The LEISA flux data has radiance units of ergs/s/cm²/Å/str, which was converted into units of

Figure 9: (Left)The measured spectrum of Vega with its original units (before conversion). (Right) The measured spectrum of Vega with converted units. The errors for the LEISA data was given in Extension 5 of the FITS file.

nW/m^2/sr. I did this by using the conversion factors in Equations 14 and 15. Equation 16 shows the general formula after combining the steps outlined in Equations 14 and 15. Figure 9 shows plots of the original and converted flux versus wavelength in microns. Notice that the flux values are on the scale of around 10^7 nW/m^2/sr.

Kurucz Vega Model

The next step after completing our PSF photometry is to calibrate the data using an accepted model of Vega's spectrum. In this case, we use the TRDS version of the Kurucz 1993 model[25]. The Kurucz 1993 ATLAS contains about 7600 stellar atmosphere models, one of them being Vega.
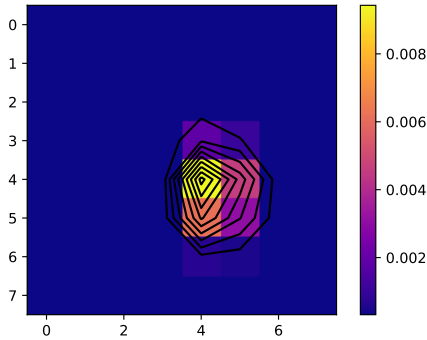

Figure 10: The fitted Gaussian for one of the stamps represented with contour lines. From this, the FWHM was extracted.

The flux data in the Kurucz Vega model[25] has units of ergs/cm^2/s/Å. I needed to convert this into units of nW/m^2/sr (sr is steradian). I used a similar approach that I used for the LEISA conversion except I had to divide each value by the solid angle of the beam

to get the sr^{-1}. The beam is a term to describe the area on the sky in which radiation will be detected by the instrument. In this case, the beam describes the width of the PSF because that is what we weighted our flux measurements by. The solid angle of the beam was calculated by taking the integral of the 2-D Gaussian with the full width at half maximum (FWHM) as the width parameter rather than the standard deviation σ. The resulting equation is shown in Equation 17.

$$\Omega = 1.13 \times (FWHM)^2 [sr/beam] \tag{17}$$

Where FWHM is the full width at half maximum of the star Vega in LEISA's image in units of radians. To find the FWHM, I first fit a 2D Gaussian to Vega in each stamp and took the average FWHM of the stamps. One of the fitted Gaussians is shown in Figure 10. To convert the FWHM from pixels to radians, I multiplied it by the single pixel field of view 60.83×10^{-6} rad (listed in Table I). Equation 18 shows the general formula used to convert the flux into the appropriate units.

$$\lambda I_{final} = \frac{I_{initial} \times \lambda[\text{Å}] \times 10^6}{\Omega} [\text{nW/m}^2/\text{sr}] \tag{18}$$

Figure 12 shows the plot of the converted model flux versus wavelength in microns. This flux is on the scale of 10^8, which is about an order of magnitude greater than the flux I calculated with LEISA. This comparison is better seen in Figure 11.

Scaling LEISA to Kurucz

As stated before, I could not successfully get the LEISA data to match with the Kurucz model as they differ by about an order of magnitude. I was unable to account for the disparity because the LEISA documentation was not clear on how the calibration of the data
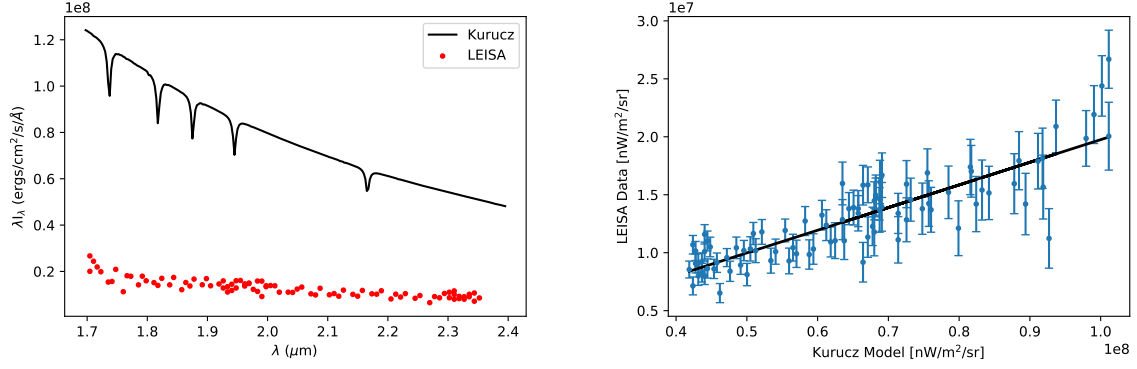
Figure 11: (Left)Comparison of the converted LEISA and Kurucz data. They differ by about an order of magnitude. The errors were omitted to better show the disparity. (Right) The converted LEISA data vs. the converted Kurucz model. The fitted line yielded a slope of 0.20 ± 0.01 and an offset of $(2.29 \pm 0.08) \times 10^5 \, \text{nW/m}^2/\text{sr}$. These values were used to scale the LEISA data to the Kurucz model.
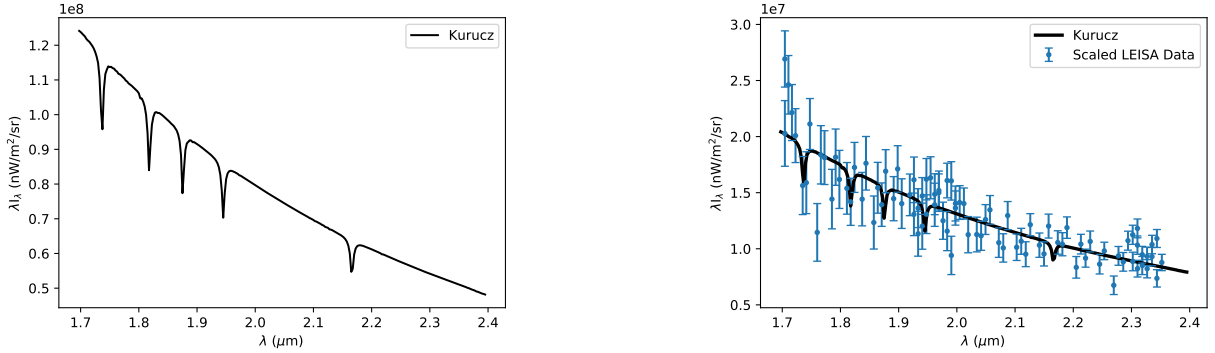

Figure 12: The model of Vega's spectrum with converted units. The flux values are about an order of magnitude greater than the LEISA flux.

Figure 13: The LEISA data and Kurucz model scaled together. Taking the RMS of the data points yields a result of about $2 \times 10^6 \, \text{nW/m}^2/\text{sr}$.

was conducted. The only way to make progress on this front is to contact the LEISA team and inquire on how they performed their calibration to make sure we agree. Due to time constraints, my advisor and I were unable to establish a working dialogue with the LEISA team and had to work around the issue ourselves.

To work around this problem, I plotted the LEISA data vs. the Kurucz data and fit a line to the data. From this line, the slope was found to be 0.20 ± 0.01 and the vertical offset to be $(2.29 \pm 0.08) \times 10^5 \, \text{nW/m}^2/\text{sr}$. This line is shown in Figure 11. After multiplying the kurucz flux by the slope and adding the offset to the LEISA data, the two sets of data matched up quite well. Figure 13 shows the two data sets plotted on the same graph.

LEISA Sensitivity Results

From the scaled values, I took the difference between each pair of data points and computed the root mean square (RMS) of the data. I found the RMS to be about $2 \times 10^6 \, \text{nW/m}^2/\text{sr}$. This value represents LEISA's sensitivity to diffuse brightness, which essentially precludes the possibility of reaching EBL signals of about $10 \, \text{nW/m}^2/\text{sr}$.

Exploring MVIC

After concluding that LEISA is not able to measure the faint EBL, we turned to another Ralph instrument: MVIC. The MVIC focal plane consists of a customized front side illuminated CCD array provided by E2V Corp. of Chelmsford, England[10]. The array has two redundant 5024×32 pixel panchromatic delay and integrate (TDI) CCDs, four 5024×32 pixel color TDI CCDs, and one 5024×264 pixel frame transfer CCD on a single substrate[12]. Together, these CCDs cover a wavelength range of 400-975nm. The four color TDI CCDs are as follows: Blue (400-550nm); Red (540-700nm); NIR(780-
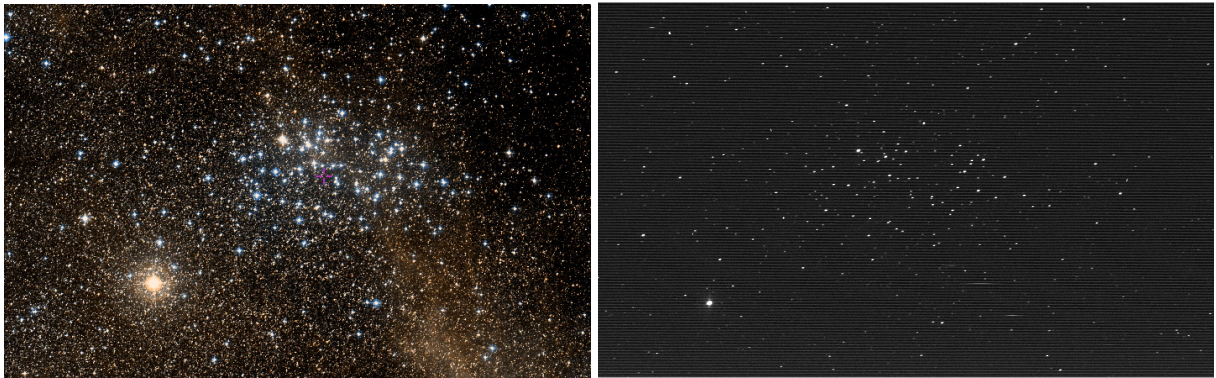
Figure 14: (Left) An image of NGC 3532, also known as the wishing well star cluster, taken from the Aladin Sky Atlas[26]. (Right) A cropped image of the same star cluster taken by MVIC. The actual length of the image is about 4 times as long. Many of these stars are of magnitude 6-10, which shows that MVIC has the ability, unlike LEISA, to detect such stars.

975nm); Methane (860-910nm)[10]. These CCDs together cover much of the optical and near-IR bands of the electromagnetic spectrum. The first and last 12 pixels of each row are not optically active, so the TDI CCDs have a 5000×32 pixel photoactive area while the pixel frame transfer CCD has a 5000×128 pixel photoactive area.

MVIC Instrument Parameters	
TDI array FOV:	5.7° × 0.037°
Framing camera FOV:	5.7° × 0.146°
Single Pixel FOV:	4.08 arcsec × 4.08 arcsec
Pixel Size:	$13\mu m$ × $13\mu m$ Pixels
Frame transfer integration time:	0.25-10s

Table II: Tabulated parameters for MVIC. All values were found in the Ralph instrument paper[10].

There are a few reasons why MVIC could potentially be used to probe the EBL. One being that MVIC exposure times are much longer than LEISA's images, ranging from 0.25-10 second exposures, depending on the type or function of the image. Another reason is that it spans a longer wavelength range, which could provide a more comprehensive spectrum of the EBL. Figure 14 shows a portion of the image mc0_0235139809_0x536_sci, which features NGC 3532, otherwise known as the wishing well star cluster. Many of the stars pictured have magnitudes of around 7. For example, one star in the cluster shown in Figure 14 is called HD96544[27] and has a B magnitude of 7.3. This demonstrates that unlike LEISA, MVIC can detect such stars.

MVIC Data Cuts

For this stage, we focused on the archival MVIC data set taken during the Pluto Cruise phase of the New Horizons mission[13]. This data set is desirable because it does not contain bright objects like planets such as Pluto or Jupiter that would pollute the image and prevent us from measuring the faint EBL. In a similar manner to LEISA, I prioritized MVIC data that have longer exposures to ensure it will be able to detect fainter signals. So my first step was to isolate all images that had exposure times greater than 5 seconds. We also wanted eliminate any images from the panchromatic TDI CCDs because the color TDI CCD images have narrower wavelength ranges, providing more data in each band of said wavelengths.

This left us with various different types of images with descriptions such as: Functional test of Ralph instrument, MVIC stellar calibration, etc. The only type of image among these that we filtered out were images with the description "Characterize Solar Scattered Light". This is because these images were more likely to be pointed at or near the sun, which is a bright foreground that may drown out the EBL signal. After completing these data cuts, I was left with 153 images. The next step was to find astrometric data for each pixel in the images.

MVIC Astrometry and Results

As stated before, pointing data is extremely important because it allows us to use star catalogues to locate stars on the image ans mask them. As with LEISA, MVIC also has an extension in each FITS image that contains a quaternion for each frame. These quaternions do not seem to have the same issue as LEISA (they each contain a nonzero z-component). However, MVIC FITS files do not contain an extension with the pointing vectors of each pixel, which means we can not use the quaternions. Without any additional information found in the documentation of the instrument, we have failed to find a way to use the quaternions to calculate the instrument pointing in the J2000 reference frame.

One other method to find astrometric data that we tried was to upload the FITS files to astrometry.net[28]. Astrometry.net is a "astrometric calibration service to

create correct, standards-compliant astrometric metadata for every useful astronomical image ever taken, past and future, in any state of archival disarray"[28]. After uploading multiple different FITS files to this online service, it was unable to provide astrometric data for any of the images.

The astrometry of MVIC could not be completed within the time allotted for this capstone project. Because of this, a sensitivity estimate for MVIC was also not able to be completed. For now, MVIC still stands as a potential tool to probe the faint EBL. Should someone continue this project, they would need to determine the pointing data of the MVIC images and mask the stars in order to begin the process of making a measurement of the EBL.

* Rochester Institute of Technology, School of Physics and Astronomy, Faculty Advisor: Michael Zemcov

1 Cooray, A. (2016). Extragalactic background light measurements and applications. Royal Society Open Science, 3(3), 150555. doi: 10.1098/rsos.150555

2 Zemcov, Michael, and Teresa Symons. *The Optical Background with New Horizons*. pp. 1–15.

3 Leinert, C. (1998). *The 1997 reference for diffuse sky brightness*. Astronomy and Astrophysics Supplementary Series, 1–99.

4 Zemcov, M., Arcavi, I., ... Werner, M. (2018). *Astrophysics with New Horizons: Making the Most of a Generational Opportunity*. Publications of the Astronomical Society of the Pacific, 130(993), 115001.

5 Dwek, E., & Hauser, M. G. (1998). The COBE Diffuse Infrared Background Experiment Search for the Cosmic Infrared Background. IV. Cosmological Implications. The Astrophysical Journal, 106–122. doi: 10.1086/306381

6 Bernstein, R. A. (2007). *The Optical Extragalactic Background Light: Revisions and Further Comments*. The Astrophysical Journal, 666(2), 663–673. doi: 10.1086/519824

7 Zemcov, M., Immel, P., Nguyen, C., Cooray, A., Lisse, C., & Poppe, A. (2016). *Measurement of the cosmic optical background using the long range reconnaissance imager on New Horizons*. Nature Communications, 1–7.

8 Matsumoto, T., Matsuura, S., ... Noda, M. (2005). Infrared Telescope in Space Observations of the Near-Infrared Extragalactic Background Light. The Astrophysical Journal, 626(1), 31–43. doi: 10.1086/429383

9 National Aeronautics and Space Agency.(2015). *New Horizons the First Mission to the Pluto System and Kuiper Belt*[Fact Sheet]. Retrieved from `https://www.nasa.gov/sites/default/files/atoms/files/nh-fact-sheet-2015_1.pdf`

10 Reuter, D., Stern, A., ... Scherrer, J. (2008). *Ralph: A Visible/Infrared Imager for the New Horizons Pluto/Kuiper Belt Mission*. Space Science Review, 129–154.

11 Keeter, Bill. *Pluto through a Stained Glass Window: a Movie from the Edge of Our Solar System*. NASA, 24 Dec. 2015, `blogs.nasa.gov/pluto/2015/12/24/pluto-through-a-stained-glass-window-a-movie-from-the-edge-of-our-solar-system/`.

12 McCabe, George, and Allen Lunsford. "New Horizons SOC to Instrument Pipeline ICD." Retrieved from `pds-rings.seti.org/newhorizons/SOC_INST_ICD.PDF`.

13 "NASA PDS: Small Bodies Node." SBN Mission Support: New Horizons, `pds-smallbodies.astro.umd.edu/data_sb/missions/newhorizons/index.shtml`.

14 "NASA PDS: Small Bodies Node." SBN Mission Support: New Horizons Kuiper Belt Extended Mission, `pds-smallbodies.astro.umd.edu/data_sb/missions/nh-kem/index.shtml`.

15 Beckett, Martin. "Rockwell PICNIC Array." Rockwell PICNIC Array, `people.ast.cam.ac.uk/~optics/tech/hawaii/picnic.htm`.

16 Souza, R. A., et al. "CMOS Image Sensor with FPN Reduction by Correlated Double Sampling in Current Mode." 2016 31st Symposium on Microelectronics Technology and Devices (SBMicro), 2016, doi:10.1109/sbmicro.2016.7731351.

17 "Image Description Files." BIL, BIP, and BSQ Raster Files-Help — ArcGIS for Desktop,`desktop.arcgis.com/en/arcmap/10.3/manage-data/raster-and-images/bil-bip-and-bsq-raster-files.htm`.

18 Gaia Collaboration, Gaia Data Release 2. Summary of the Contents and Survey ... `ui.adsabs.harvard.edu/abs/2018A&A...616A...1G/abstract`.

19 "Cosmic Coordinates." Las Cumbres Observatory, lco.global/spacebook/sky/equatorial-coordinate-system/.

20 Yang, Yaguang. "Spacecraft Attitude Determination." Spacecraft Modeling, Attitude Determination, and Control Quaternion-Based Approach, 2019, pp. 65–82., doi:10.1201/9780429446580-6.

21 Bohlin, R. C., and R. L. Gilliland. "Hubble Space TelescopeAbsolute Spectrophotometry of Vega from the Far-Ultraviolet to the Infrared." The Astronomical Journal, vol. 127, no. 6, June 2004, pp. 3508–3515., doi:10.1086/420715.

22 Bertin, Emmanuel. SExctractor v2.5 User's Manual. Institut d'Astrophysique & amp; Observatoire De Paris.

23 Stetson, P. B. (1987). DAOPHOT - a computer program for crowded-field stellar photometry. Publications of the Astronomical Society of the Pacific, 99, 191-222. doi:10.1086/131977

24 Building an effective point spread function (epsf) (n.d.). Retrieved May 02, 2021, from `https://photutils.`

[25] `readthedocs.io/en/stable/epsf.html#build-epsf`
Kurucz 1993 Models. (n.d.). Retrieved May 02, 2021, from `https://www.stsci.edu/hst/instrumentation/reference-data-for-calibration-and-tools/astronomical-catalogs/kurucz-1993-models`

[26] Aladin Sky Atlas, `aladin.u-strasbg.fr/AladinDesktop/#Description`.

[27] "SIMBAD Query Result." SIMBAD Astronomical Database - CDS (Strasbourg), `simbad.u-strasbg.fr/simbad/sim-id?Ident=HD%2B%2B96544`.

[28] Astrometry.net. (n.d.). Retrieved May 02, 2021, from `http://astrometry.net/`